High Power Laser Science and Engineering, (2023), Vol. 11, e88, 10 pages.
doi:10.1017/hpl.2023.72

HIGH POWER LASER SCIENCE AND ENGINEERING

RESEARCH ARTICLE

Experimental investigation of the stimulated Raman scattering effect in high-power nanosecond superfluorescent fiber source

Chaoyu Ning[1,2,3,4,†], Shuzhen Zou[1,4,†], Haijuan Yu[1,2,3,4], Jiexi Zuo[1,2,3,4], Xuechun Chen[1,2,3,4], Shuang Xu[1,2,3,4], Shifei Han[1,2,3,4], Xinyao Li[1,2,3,4], Wenjuan Wu[1,2,3,4], Chaojian He[1,4], and Xuechun Lin[1,2,3,4]

[1] *Laboratory of All-Solid-State Light Sources, Institute of Semiconductors, Chinese Academy of Sciences, Beijing, China*

[2] *Center of Materials Science and Optoelectronics Engineering, University of Chinese Academy of Sciences, Beijing, China*

[3] *College of Materials Science and Opto-Electronic Technology, University of Chinese Academy of Sciences, Beijing, China*

[4] *Beijing Engineering Technology Research Center of All-Solid-State Lasers Advanced Manufacturing, Beijing, China*

(Received 11 May 2023; revised 20 July 2023; accepted 22 August 2023)

Abstract

In this work, we experimentally investigate the dependence of the stimulated Raman scattering (SRS) effect on the seed linewidth of a high-power nanosecond superfluorescent fiber source (ns-SFS). The results reveal that the SRS in the ns-SFS amplifier is significantly influenced by the full width at half maximum (FWHM) of the ns-SFS seed, and there is an optimal FWHM linewidth of 2 nm to achieve the lowest SRS in our case. The first-order SRS power ratio increases rapidly when the seed's linewidth deviates from the optimal FWHM linewidth. By power scaling the ns-SFS seed with the optimal FWHM linewidth, a narrowband all-fiberized ns-SFS amplifier is achieved with a maximum average power of 602 W, pulse energy of 24.1 mJ and corresponding peak power of 422.5 kW. This is the highest average power and pulse energy achieved for all-fiberized ns-SFS amplifiers to the best of our knowledge.

Keywords: fiber amplifier; high power; nanosecond superfluorescent fiber source; stimulated Raman scattering effect

1. Introduction

Pulsed fiber lasers with conspicuous conversion efficiency, compactness and reliability have gained widespread attention in laser processing, nonlinear frequency conversion, coherent beam combining and other applications[1–4]. In particular, all-fiberized nanosecond pulsed amplifiers with high power and large energy are desired in varied applications, such as laser ablation and surface treatments[5,6]. Typically, high-power all-fiberized nanosecond pulsed amplifiers employ a master oscillator power amplifier (MOPA) configuration where the nanosecond fiber seed is achieved via a *Q*-switched regime or external modulation of a continuous-wave fiber laser[7,8]. However, the stochastic self-pulsing and the interactions of longitudinal modes inherent in fiber oscillators degrade their temporal stability and the threshold of the nonlinear effects, thereby limiting the average power and pulse energy of all-fiberized pulsed amplifiers[8–10]. In addition, all-fiberized nanosecond pulsed amplifiers with low coherence are demanded in the high-quality full-field imaging of dynamic targets on the nanosecond timescale and in other applications[11]. Therefore, it is significant to develop a fiber seed that improves temporal stability and unlocks the application potential of high-power nanosecond pulsed amplifiers.

The superfluorescent fiber source (SFS) derives from the superfluorescent radiation in the active fiber, which has unique features such as broadband emission, low coherence and high temporal stability[12–14]. The pursuit of high-power SFS amplifiers has emerged as a research frontier, owing to their potential for diverse applications such as the generation of mid-infrared laser and supercontinuum sources, the pumping of Raman fiber lasers and material processing[15–17]. Due to the absence of a resonant cavity structure, the SFS can effectively avoid the self-pulsing and the interactions of longitudinal modes, improving the temporal stability and exhibiting remarkable advantages in nonlinear effects suppression[18–21]. Thus, the nanosecond fiber seed

Correspondence to: Xuechun Lin, Laboratory of All-Solid-State Light Sources, Institute of Semiconductors, Chinese Academy of Sciences, Beijing 100083, China. Email: xclin@semi.ac.cn

[†]These authors contributed equally to this work.

generated by externally modulated SFS can resolve the temporal instability issues associated with the resonant cavity structure-based nanosecond fiber seed. However, demonstrations of high-power SFS amplifiers have predominantly focused on continuous-wave SFSs[22–26], with reports on pulsed SFS amplifiers featuring high average power and large pulse energy being relatively scarce. Park *et al*.[19] reported a narrowband nanosecond superfluorescent fiber source (ns-SFS) with an average power of 41.5 W, pulse energy of about 0.4 mJ and pulse width of 26.4 ns, while pulsed SFS amplifiers delivering average power at the hundred-watt level and pulse energy at the approximately 10 mJ level have yet to be reported. In addition, the scaling of average power and pulse energy in all-fiberized nanosecond amplifiers is primarily limited by amplified spontaneous emission (ASE) and nonlinear effects, particularly stimulated Raman scattering (SRS)[27]. In addition, recent research indicates that the SRS in continuous-wave fiber lasers is significantly related to the spectral width. For instance, Schreiber *et al*.[28] reported that the threshold of SRS for fiber oscillators depends on the spectral width of the out-coupling fiber Bragg grating (FBG), while Liu *et al*.[29] demonstrated that the SRS in a narrowband filtered SFS is enhanced rapidly with the narrowing of the seed's linewidth. Besides, Bock *et al*.[30] fully explained the observed SRS enhancement for spectrally narrower fiber laser systems. Hence, investigating spectral evolution to inhibit SRS is a promising approach for achieving high output power and large pulse energy of all-fiberized ns-SFS amplifiers.

In this work, we obtain the nanosecond fiber seed by an externally modulated SFS and investigate the impact of the seed's linewidth on SRS in an ns-SFS amplifier for the first time. Our experimental findings indicate that the SRS in the ns-SFS amplifier is significantly influenced by the full width at half maximum (FWHM) linewidth of the ns-SFS seed. Specifically, when the seed's linewidth is less than or greater than 2 nm, the first-order SRS power ratio in the ns-SFS amplifier grows rapidly at a specific pump power. Since the ns-SFS seed with an FWHM linewidth of 2 nm exhibits the best SRS suppression, we amplify its average power and pulse energy. At this point, the amplified ns-SFS attains a maximum average power of 602 W, a pulse width of 57 ns, a pulse energy of 24.1 mJ and a peak power of 422.5 kW. This is the highest average power and pulse energy for all-fiberized ns-SFS amplifiers ever reported.

2. Experimental setup

2.1. The nanosecond pulsed superfluorescent fiber source

The experimental setup utilized in this study comprises a typical MOPA configuration, mainly comprising a low-power ns-SFS seed and three-stage amplifiers. As shown in Figure 1, the ns-SFS seed consists of an SFS, a pre-amplifier and a spectral filtering cell. The SFS is pumped by a 9 W 976 nm laser diode (LD). The pumping light is coupled into an 11 m double-cladded Yb-doped fiber (YDF) using a $(2 + 1) \times 1$ signal/pump combiner. The active fiber has a core diameter of 10 μm, an inner cladding diameter of 125 μm and a cladding absorption coefficient of 1.65 dB/m at 915 nm. The end of the backward output is cleaved at an 8° angle to reduce the feedback along the fiber. In the meantime, the forward output of the SFS is modulated by an acoustic-optical modulator (AOM 1) to generate nanosecond pulses. After AOM 1, the generated nanosecond pulses are directed into the pre-amplifier via a $(2 + 1) \times 1$ signal/pump combiner, where the active fiber has the same parameters as the SFS and is 6 m in length. A 976 nm LD also pumps the pre-amplifier with a maximum power of 9 W. The amplified nanosecond pulses are then launched into

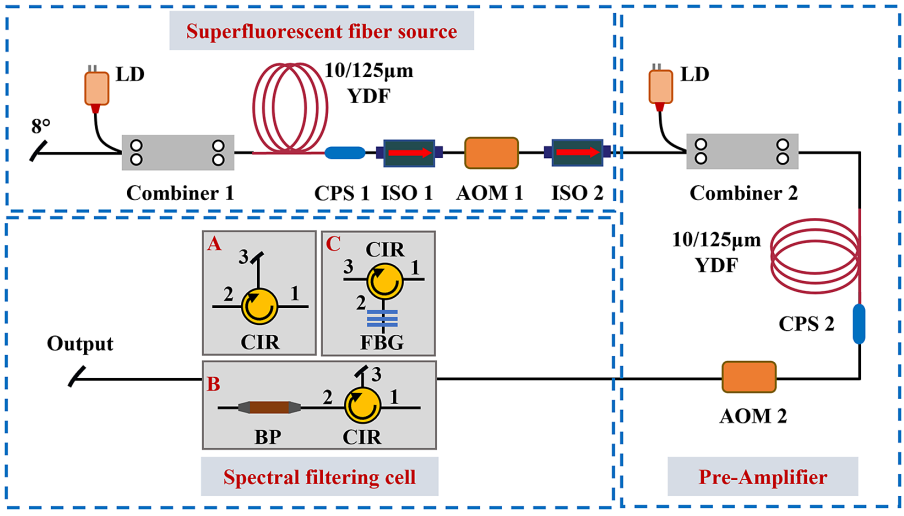

Figure 1. The experimental setup of the ns-SFS seed.

https://doi.org/10.1017/hpl.2023.72 Published online by Cambridge University Press

AOM 2, the same as AOM 1, to enhance the extinction ratio. Notably, AOM 1 and AOM 2 are synchronized by an arbitrary waveform generator (AWG). The spectrum of the pulsed SFS is modulated in the spectral filtering cell after AOM 2. In the spectral filtering cell, three schemes are implemented. Scheme A allows the pulsed SFS to pass only through a circulator (CIR) without spectral filtering. Scheme B employs a bandpass filter (BP) to achieve the pulsed SFS with an FWHM linewidth of 8 nm, while Scheme C utilizes FBGs with different linewidths to obtain a pulsed SFS with FWHM linewidths of 0.25, 0.5, 1, 2, 3 and 5 nm. In addition, fiberized isolators (ISOs) and homemade cladding pump strippers (CPSs) are used in each stage to safeguard the preceding stage and dump the light in the cladding.

Experimentally, by employing the AWG to set the drive signals of AOM 1 and AOM 2, the ns-SFS with a pulse width of 255 ns and repetition frequency of 25 kHz is generated after the pre-amplifier. The spectrum of the ns-SFS is then manipulated in the spectral filtering cell. Figure 2(a) illustrates that the spectral range of the unfiltered ns-SFS spans from 1025 to 1123 nm, featuring a central wavelength of 1069.8 nm and an FWHM of 14 nm. In addition, the spectra of the ns-SFS filtered by Schemes B and C are shown in Figure 2(b), where the legend represents the FWHM linewidth of the filtered spectrum, with all filtered ns-SFSs having a central wavelength of approximately 1064 nm. Furthermore, Figure 2(c) demonstrates that the intensity-normalized pulse profiles of the unfiltered ns-SFS and filtered ns-SFSs are nearly identical, exhibiting a pulse width of approximately 255 ns. However, the peak of the pulse profiles exhibits different temporal fluctuations. In addition, the pulse peaks in Figure 2(c) are separated by intensity bias to illustrate the details of the fluctuations at the pulse peak of the ns-SFS seed, as shown in Figure 2(d). The results indicate that the temporal fluctuations of the pulse peak are weak when the FWHM linewidth is larger than 2 nm, but are significantly strengthened when the FWHM linewidth is smaller than 2 nm. Thus, the wideband ns-SFS seed can effectively resolve issues such as self-pulsing commonly observed in oscillator-based fiber seeds[9,10], while extensive

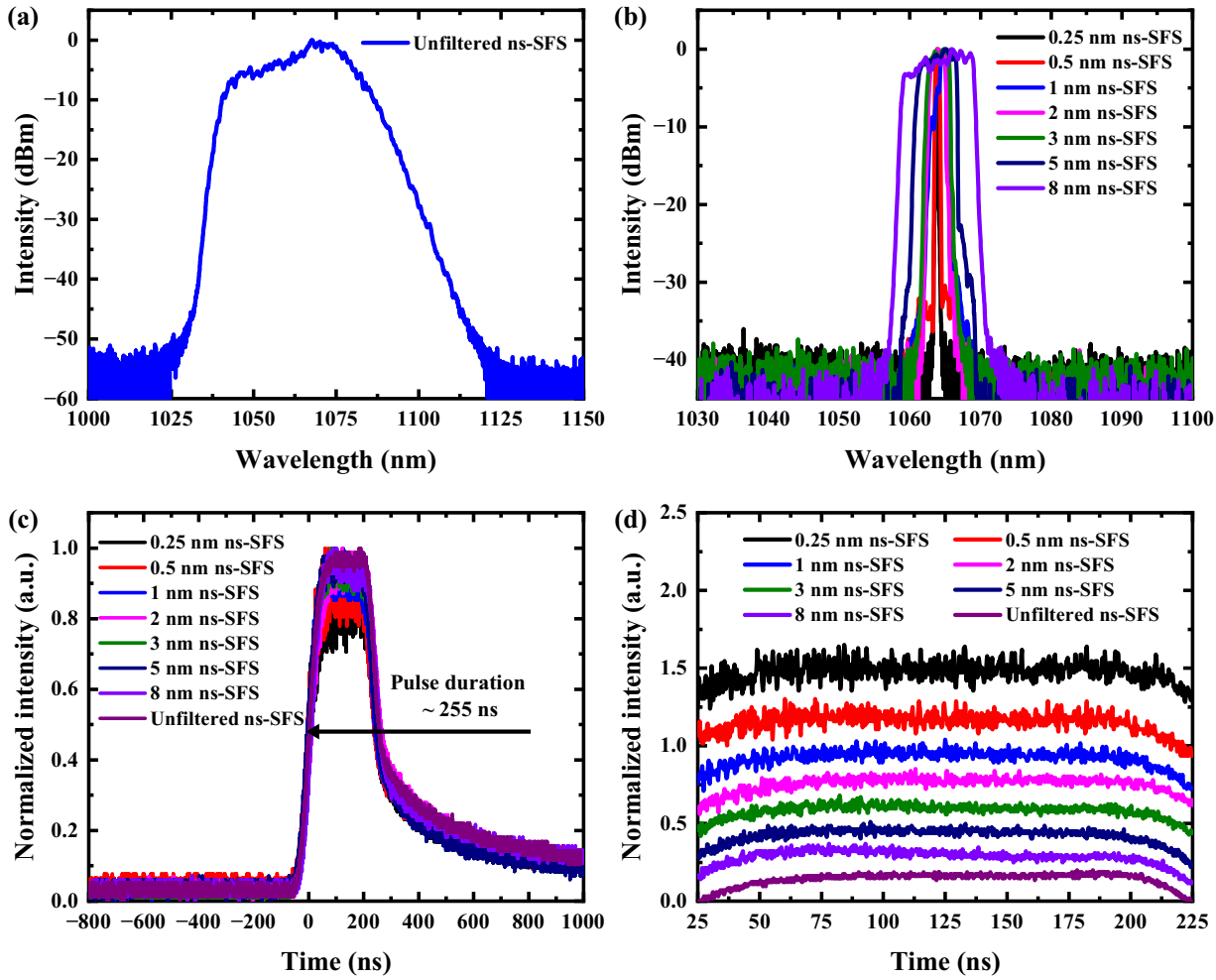

Figure 2. The output characteristics of the ns-SFS seed. The output spectra of the unfiltered ns-SFS (a) and the filtered ns-SFSs (b). (c) The pulse profiles. (d) The fluctuations at the pulse peak of the ns-SFS seed.

https://doi.org/10.1017/hpl.2023.72 Published online by Cambridge University Press

Table 1. Output power of the ns-SFS seed versus the FWHM linewidth.

Seed linewidth (nm)	Output power (mW)	Seed linewidth (nm)	Output power (mW)
Unfiltered ns-SFS	445.0	2	22.4
8	133.1	1	11.5
5	36.6	0.5	5.7
3	30.8	0.25	3.0

spectral filtering also leads to a degradation in the temporal stability of the ns-SFS seed.

Moreover, the average power of the ns-SFS obtained by AOM 1 modulation is 2.3 mW. After the pre-amplifier and spectral filtering cell, the average output power of the unfiltered ns-SFS is amplified to around 445 mW. However, the spectral narrowing of the seed by spectral filtering results in average power loss, yielding output power ranging from 133.1 mW for an 8 nm ns-SFS to 3.0 mW for a 0.25 nm ns-SFS (see details in Table 1).

2.2. *Power amplifiers*

To further increase the output power of the ns-SFS, the pulses are injected into two booster amplifiers for preamplification, and finally the power is amplified by a main amplifier (see Figure 3). The components used in the first booster amplifier are the same as those used in the pre-amplifier of the ns-SFS seed, except for the absence of an AOM and the utilization of a 2.5 m long active fiber in the first booster amplifier. The second booster amplifier is constructed using a 2.8 m long YDF with core/inner cladding diameters of 30/250 μm, pumped by a 60 W fiber-pigtailed 976 nm LD through a $(2 + 1) \times 1$ signal/pump combiner. For the main amplifier, a 2 m long YDF is employed with core/inner cladding diameters of 100/400 μm (core NA 0.11, absorption coefficient of approximately 6 dB/m at 915 nm). Six 976 nm LDs with a maximum output power of 180 W are used to pump the active fiber of the main amplifier via a $(6 + 1) \times 1$ signal/pump combiner. Besides, to better investigate the influence of the ns-SFS seed's FWHM linewidth on SRS, a 15 m-long passive fiber (GDF) matched with the active fiber of the main amplifier in size is employed to heighten the SRS. A fiber-pigtailed end cap is applied at the end of the system to avoid unexpected end reflection and fiber facet damage. Meanwhile, the ISO and CPS are arranged at every stage to protect the preceding stage from damaging and dump the residual pump light. Apart from the fiber-pigtailed end cap, all the other optical components are mounted on water-cooled heat sinks.

In our all-fiberized ns-SFS MOPA system, the following instruments are utilized to characterize its performance: a water-cooled power meter to measure the average power, a digital oscilloscope (Keysight MSOX3104T) with a sampling rate of 5 GS/s to observe the pulse profile and an optical spectrum analyzer (Yokogawa AQ6370D) with a minimum resolution of 0.02 nm to analyze the amplified ns-SFS spectra.

3. Results and discussion

3.1. *SRS effect in the ns-SFS amplifier with various seed linewidths*

3.1.1. *Amplification of the ns-SFS seed with different linewidths*

To study the amplification characteristics and the SRS inhibition ability of the ns-SFS seed with different FWHM linewidths, we experimentally investigate the power scaling of the filtered ns-SFS seeds. To ensure the accuracy of the results, we first compare the output characteristics of the booster amplifiers. All filtered ns-SFS seeds have a repetition frequency of 25 kHz and a pulse width of approximately

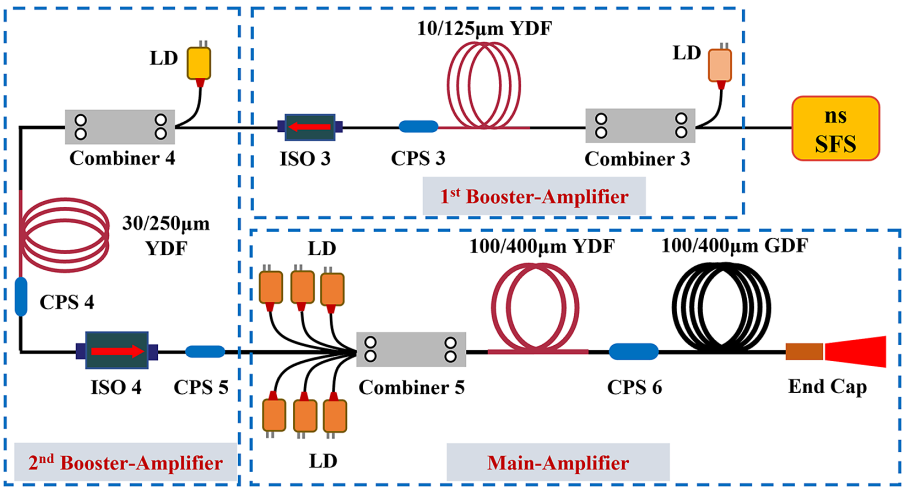

Figure 3. The experimental setup of the ns-SFS amplifier.

https://doi.org/10.1017/hpl.2023.72 Published online by Cambridge University Press

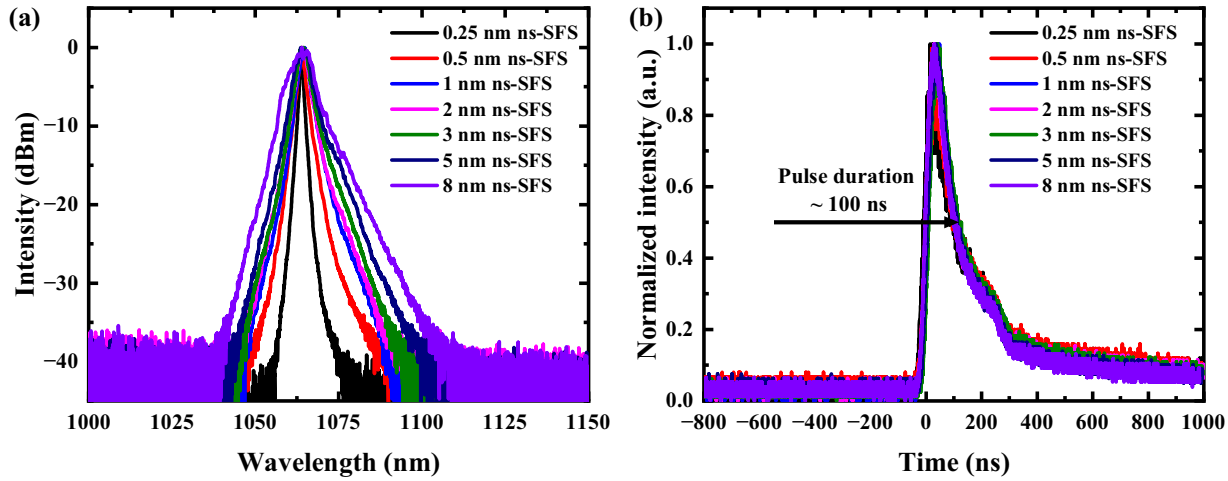

Figure 4. The output spectra (a) and the pulse profiles (b) of the ns-SFS signals at an output power of approximately 18 W.

255 ns (see Figure 2(c)). The average output power of the filtered ns-SFSs can be amplified to 1 W by the first booster amplifier and then be amplified to about 18 W by the second booster amplifier. The spectra of the amplified ns-SFS with an output power of 18 W after two booster amplifiers are shown in Figure 4(a). The central wavelength of all filtered ns-SFS signals remains at about 1064 nm, while the spectral range is significantly widened due to the onset of nonlinear effects, such as the self-phase modulation (SPM). On the other hand, as shown in Figure 4(b), the pulse profiles of the amplified ns-SFSs with an average power of 18 W are nearly identical, where the pulse widths are compressed from approximately 255 ns to approximately 100 ns owing to pulse distortion[31]. Therefore, the filtered ns-SFS signals have a similar pulse profile, pulse width, output power and pulse energy before entering the main amplifier, which can ensure the reliability of the results of the amplified ns-SFS signals in the main amplifier.

After the first and second booster amplifiers, we inject 18 W output power of filtered ns-SFSs into the main amplifier as the signal to explore power scalability and SRS effect. In Figure 5(a), it can be observed that the output power of the ns-SFS signals grows linearly as the pump power increases in all cases. Specifically, a maximum average power of about 265 W is achieved at a pump power of 370 W for all filtered ns-SFS signals, resulting in an optical-to-optical efficiency of about 68% and a pulse energy of about 10.6 mJ. The further power scaling of these ns-SFS signals is restricted by the SRS, which is enhanced by the long passive-matched fiber (see Figure 6 for details). The low optical-to-optical efficiency of the ns-SFS signals can be attributed to the transfer of the signal power to the Raman Stokes light. Figure 5(b) displays the pulse width of the amplified ns-SFSs versus the pump power. The pulse width of the signals entering the main amplifier is nearly identical for all cases, with the value of about 100 ns. In addition, the maximal deviation of the pulse widths between the highest and lowest values is less than 2.5 ns. As the pump power increases, the pulse width of the seven ns-SFS signals gradually narrows. At a pump power of 370 W, the pulse duration of the seven ns-SFS signals is narrowed to about 67 ns with a maximal deviation of less than 1.0 ns. Figure 5(c) presents the pulse profiles of the seven ns-SFS signals at a pump power of 370 W. Although there is a slight difference in pulse width after amplification, the pulse profiles remain essentially the same, exhibiting a steeper leading edge than trailing edge. In addition, the temporal fluctuations of the pulse peak are stronger with the spectral narrowing of the filtered ns-SFSs at the pump power of 370 W, as demonstrated in Figure 5(d). At the maximum average power, the peak power for the seven ns-SFS amplifiers fluctuates slightly around 158 kW, with a maximum deviation of less than 4 kW between the highest and lowest values. Considering that the seven ns-SFS amplifiers exhibit nearly identical average power, pulse width and pulse profile under the same pump power, their peak power density remains almost identical.

3.1.2. Dependence of SRS on the seed linewidth in an ns-SFS amplifier

We analyze the Raman power ratio of seven ns-SFS amplifiers at varying pump powers to investigate the impact of the spectral FWHM linewidth on SRS. The strength of the SRS in a laser in different cases cannot be accurately judged only by observing the intensity of the Raman peak; rather, one has to take into account the SRS wavelength band by spectral integration to calculate its proportion in the total laser output. Specially, we selected the spectral range of 1100–1150 nm as the first-order Raman Stokes light and calculated the first-order Raman power ratio of the seven ns-SFS amplifiers via dividing the integrated Raman spectrum by the integral spectrum from 1000 to 1220 nm, as depicted in Figure 6(a). The results indicate that the first-order Raman power ratio of the seven amplifiers increases rapidly with growing pump

https://doi.org/10.1017/hpl.2023.72 Published online by Cambridge University Press

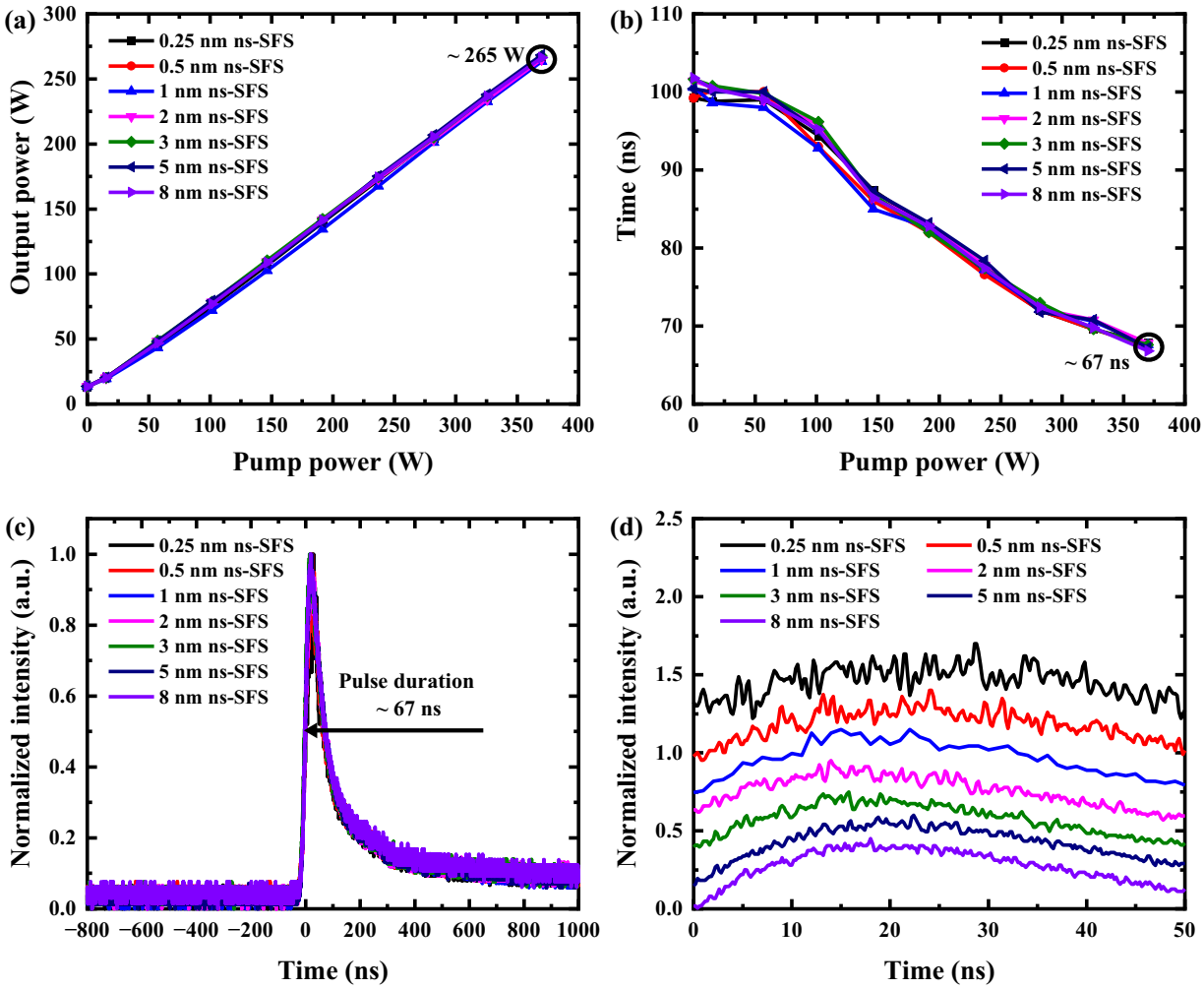

Figure 5. (a) The output power and (b) pulse width of amplified ns-SFS signals as a function of pumping power, (c) the pulse profiles and (d) the details of the pulse peak of amplified ns-SFS signals at a pump power of 370 W.

power. Notably, at the same pump power, the 2 nm ns-SFS amplifier displays the lowest first-order Raman power ratio, whereas the Raman power ratios of the ns-SFS amplifiers with seed linewidths greater than or less than 2 nm are progressively enhanced.

To investigate the relationship between the SRS and the FWHM linewidth of the ns-SFS seed in more detail, we analyze the output spectra of the ns-SFS amplifiers and the content of each spectral component under a pump power of 370 W, as depicted in Figures 6(b) to 6(d). Figure 6(b) shows the output spectra of the seven ns-SFS amplifiers at a pump power of 370 W. Because of the combination of the SPM and SRS enhanced by the long passive matching fiber, all seven ns-SFS amplifiers exhibit severe asymmetric broadening in the output spectra, as compared to the 18 W signals entering the main amplifier (see Figure 4(a)). The seven amplifiers manifest different first-order SRS content in the spectral range of 1100–1150 nm and second-order SRS content in the 1150–1220 nm range. In addition, the ASE of all ns-SFS amplifiers at 1010–1045 nm is weak.

However, the spectral broadening of the amplified laser exhibits an overlap with the SRS peak, particularly evident in the case of the 8 nm ns-SFS. To enhance the accuracy of the SRS power ratio, one potential approach involves fitting the red wavelength shoulder of the spectral broadening to establish a baseline and subsequently integrating only the portion above this baseline. Figure 6(c) shows the output spectra obtained experimentally and through fitting in the case of the 8 nm ns-SFS at a pump power of 370 W. In this instance, a first-order SRS wavelength band spanning 1100–1150 nm is fitted to establish a baseline.

According to the above method, we get an accurate first-order SRS power ratio. The dependence of the first-order SRS power ratio on the linewidth of the ns-SFS seed at a pump power of 370 W is shown in Figure 6(d). Although the peak power of all seven ns-SFS amplifiers is approximately 158 kW, their first-order SRS power ratio increases rapidly when the seed's linewidth deviates from 2 nm. When the FWHM linewidth of the ns-SFS seed is less than 2 nm, the first-order SRS power ratio increases rapidly with the

https://doi.org/10.1017/hpl.2023.72 Published online by Cambridge University Press

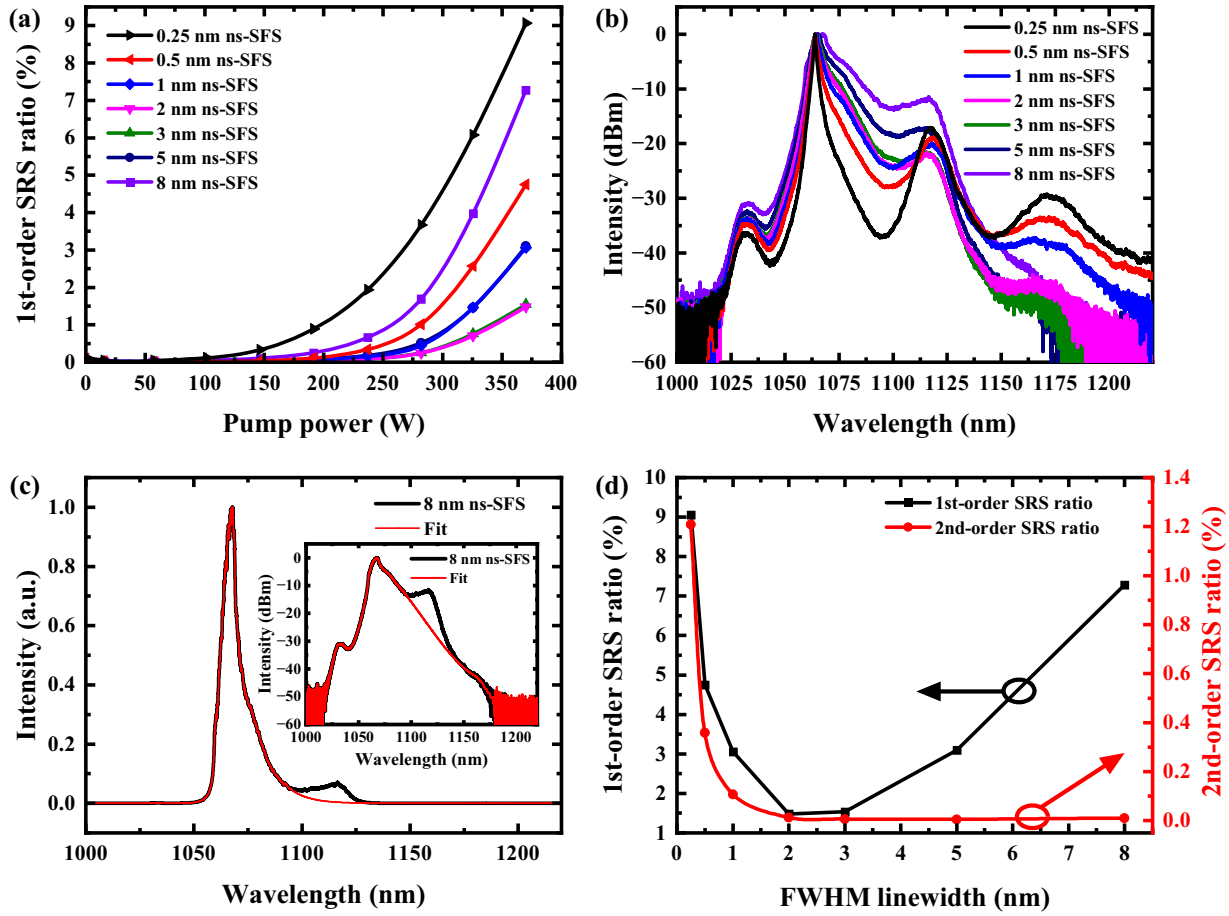

Figure 6. The SRS of the amplified ns-SFS with various linewidths. (a) The first-order SRS power ratio of seven ns-SFS amplifiers under different pump powers. (b) The output spectra of the ns-SFS amplifiers with a pump power of 370 W. (c) The experimental and fitted output spectra in the case of an 8 nm ns-SFS at a pump power of 370 W in a linear scale; inset, the corresponding spectra in a logarithmic coordinate. (d) The first-order SRS power ratio and the second-order SRS power ratio versus the ns-SFS seed's FWHM linewidth at a pump power of 370 W.

narrowing of the spectral width, consistent with the reports in Refs. [28–30]. This phenomenon may be related to the temporal fluctuations at the pulse peak of the filtered ns-SFS seed, as reported in a previous study of SRS in a narrowband SFS amplifier[29]. The temporal fluctuations at the pulse peak of the ns-SFS seed and the main amplifier become significantly stronger when the seed's linewidth is less than 2 nm (see Figures 2(d) and 5(d)). The SRS effect is closely related to the temporal characteristics of the laser, and the temporal fluctuations can increase the effective Raman gain coefficient, resulting in the early onset of the first- and second-order Stokes waves[32,33]. Therefore, these unstable pulse peaks cause the ns-SFS amplifier with an FWHM linewidth of less than 2 nm to experience more severe SRS.

Conversely, the first-order SRS power ratio increases quickly with the broadening of the spectral width when the linewidth of the ns-SFS seed is larger than 2 nm (see Figure 6(d)), in which case the fluctuations at the pulse peaks of the ns-SFS seeds and amplifiers are weak (see Figures 2(d) and 5(d)). We attribute this phenomenon to the impact of the severe SPM induced by the high peak power density of ns-SFS amplifiers on the SRS. The severe SPM results in a rapid spectral expansion on both wings of the central wavelength, even extending to the Raman wavelength band[34]. When the signal carrying the noise of the Raman wavelength band is amplified in the main amplifier, the SRS threshold will be reduced, leading to severe SRS[35,36]. It can be seen from Figure 4(a) that the wider the ns-SFS seed's FWHM linewidth, the wider the spectral range of the amplified 18 W signals due to the SPM. This indicates that the signals entering the main amplifier possess varying initial Raman band content. The first-order SRS ratio at a pump power of 0 W in Figure 6(a) represents the initial Raman band content of the signals entering the main amplifier, with values of 0.01%, 0.02%, 0.04% and 0.06% for the 2 nm ns-SFS, the 3 nm ns-SFS, the 5 nm ns-SFS and the 8 nm ns-SFS, respectively. Although the initial Raman band content of these ns-SFS signals is very low, these noise levels can affect the SRS in the main amplifier, as reported in Ref. [36]. Consequently, in the case that the linewidth of ns-SFS seed is greater than 2 nm, the spectral range of the ns-SFS signal with a wider linewidth expands

https://doi.org/10.1017/hpl.2023.72 Published online by Cambridge University Press

more easily to the first-order Raman wavelength band than that of the narrow signal (>2 nm) due to the SPM effect, resulting in higher noise content of the first-order Raman band in the signal and more severe first-order SRS after power scaling.

We also investigate the relationship between the second-order SRS power ratio and the ns-SFS seed's linewidth, as shown in Figure 6(d). Here, the ratio of the second-order SRS power to the output power is calculated through dividing the integrated spectrum from 1150 to 1220 nm by the integrated spectrum from 1000 to 1220 nm. The second-order SRS power ratio decreases rapidly with the increase of linewidth and the value approaches 0 until the linewidth is larger than 2 nm. This may be related to the pulse peak fluctuations of the ns-SFS seeds and amplifiers, which rapidly weaken with the growing linewidth when the linewidth is less than 2 nm (see Figures 2(d) and 5(d)). Then, the pulse peak fluctuations show a slight change towards a wider linewidth.

In addition, the power ratio of the ASE light to the total output is calculated by dividing the integrated spectrum from 1010 to 1045 nm by the integrated spectral range from 1000 to 1220 nm, which is called the ASE ratio for short. The dependence of the ASE ratio and spectral broadening factors on the seed's FWHM linewidth at a pump power of 370 W is shown in Figure 7. As the linewidth of the ns-SFS seed increases, the ASE ratio gradually decreases from 0.13% to 0.08%, which may be caused by the wideband ns-SFS signal consuming a more inverted population than the narrowband signal. Notably, the ASE power ratio cannot be accurately determined by comparing the peak intensity of the ASE band in the spectrum, as the optical power spectral density of output spectra with different seed linewidths is distinct. Accordingly, the ASE ratio evolution obtained by spectral integration shown in Figure 7 differs from the ASE peak intensity in the output spectrum of Figure 6(b). The spectral broadening factor is calculated via dividing the FWHM linewidth of the ns-SFS amplifier by the FWHM linewidth of the ns-SFS seed. As depicted in Figure 7, the spectral broadening factor decreases rapidly and gradually approaches 1 with the widening of the seed linewidth. This phenomenon can be understood by combining the group-velocity dispersion (GVD) and SPM effects[37]. When the ns-SFS signal has a narrow linewidth, its FWHM linewidth broadens quickly due to SPM. However, the intensity of the GVD effect is highly dependent on the spectral width. Thus, the interplay between the GVD effect and the SPM effect causes the spectrum of the ns-SFS signal with a wide linewidth to remain essentially unchanged in the central part at a specific output power. At the same time, the spectral wings will continue to broaden[38].

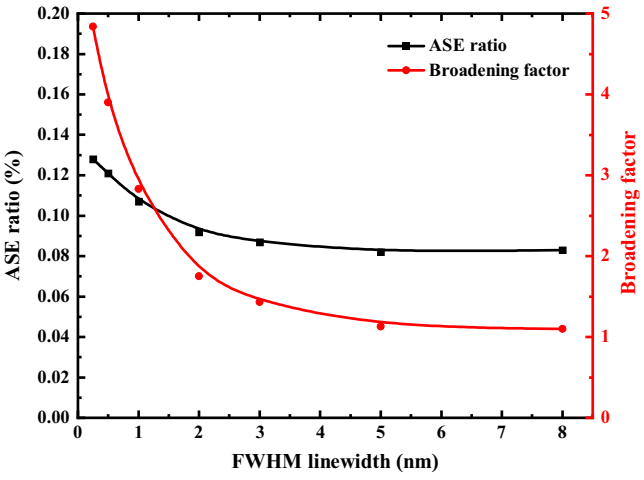

Figure 7. The dependence of the ASE power ratio and spectral broadening factor on the FWHM linewidth of the ns-SFS seed at a pump power of 370 W.

3.2. Scaling of the output power and pulse energy of the filtered ns-SFS seed

According to the above analysis, the filtered ns-SFS seed has an optimal FWHM linewidth to minimize the SRS effect, which is 2 nm in our case, allowing further scaling of the pulse energy and output power of this type of pulsed laser. Therefore, we further amplify the output power and pulse energy of the 2 nm ns-SFS seed after removing the 15 m passive matching fiber shown in Figure 3. Through the first booster amplifier, the output power of the 2 nm ns-SFS can be scaled to 1 W, which can be further boosted up to 18 W with the second booster amplifier, thereby delivering adequate signal power for the main amplifier. The dependencies of the average output power and the pulse width of the main amplifier on the pump power are shown in Figure 8(a). As the pump power increases, the average power grows nearly linearly, indicating a slope efficiency of 74.1%. However, the pulse width is gradually compressed with the scaling of the pump power due to pulse distortion[31,39,40]. As depicted in Figure 8(b), the leading edge of the pulse consumes more inversion than the trailing edge, resulting in a higher gain and gradual steepening of the leading edge and even causing pulse compression with the increasing output power. At the maximum pump power of 816.4 W, the pulse duration is narrowed to about 57 ns. Maximum average power of 602 W is achieved, corresponding to a calculated pulse energy of 24.1 mJ and a peak power of 422.5 kW. To our knowledge, this is the highest average power and largest pulse energy ever reported for an all-fiberized narrowband ns-SFS amplifier.

Figure 8(c) shows the spectra of the amplified 2 nm ns-SFS at different output powers. With the scaling of the output power, the two wings of the spectrum are gradually widened due to the onset of nonlinear effects such as the SPM. At the maximum output power of 602 W, the spectral width

https://doi.org/10.1017/hpl.2023.72 Published online by Cambridge University Press

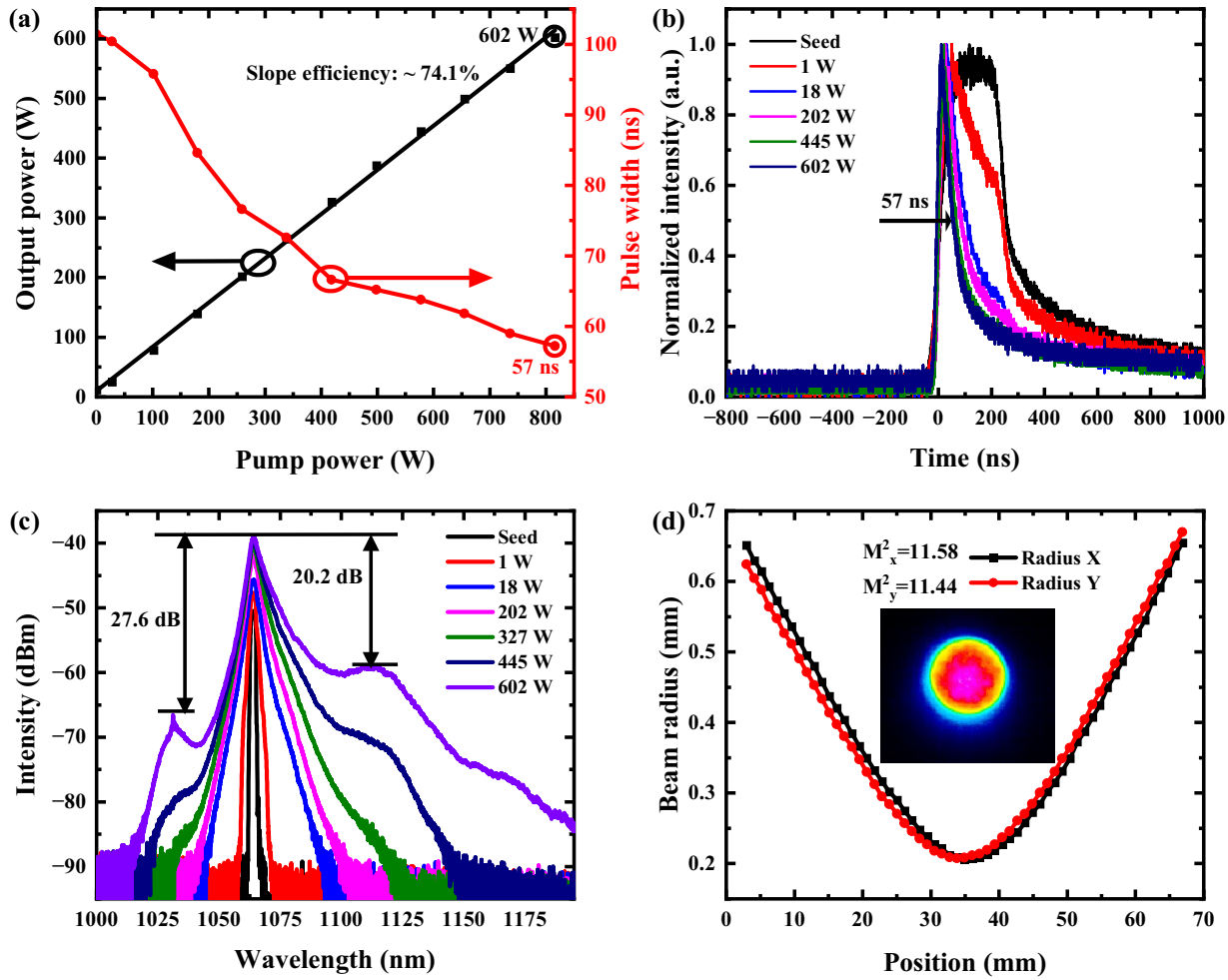

Figure 8. Output performance of the 2 nm ns-SFS amplifier. (a) Output average power (black line) and pulse width (red line) versus pump power. (b) Pulse profiles at different output powers. (c) Output spectra dependence on the operation power. (d) Beam quality at the maximum output power of 602 W.

widens to 4.1 nm and the central wavelength is 1064.5 nm. The first-order SRS and the second-order SRS wavelength bands are suppressed at 20.2 and 35 dB, respectively, while the ASE wavelength band is suppressed at 27.6 dB with a weak lasing at 1032 nm. Furthermore, the beam quality at the maximum output power of 602 W is as depicted in Figure 8(d), with the M^2 of approximately 11.51 (M_x^2 =11.58, M_y^2 =11.44). This poor beam quality can be attributed to employing gain fiber with an extra-large mode area in the main amplifier. Since the extra-large mode area of the gain fiber supports hundreds of higher-order modes, the mode mixing among these modes makes it difficult to observe the interaction between the fundamental and higher-order modes. Therefore, it is arduous to investigate the nonlinear effects related to the beam quality, such as transverse mode instability and SRS-induced mode distortion, in such a large gain fiber[41–43]. Furthermore, enhancing the beam quality of fiber laser systems with high power and large pulse energy is a crucial avenue to unlock their potential applications. The tapered fiber or chirally coupled-core fiber holds promise in achieving near-diffraction-limited beam quality of such fiber laser systems, while simultaneously addressing challenges such as transverse mode instability and SRS-induced mode distortion.

4. Conclusion

In conclusion, we first explore the relationship between the SRS effect and the seed linewidth of high-power pulsed SFS and find that there is an optimal FWHM linewidth to achieve the lowest SRS for the fiber amplifier. The optimal linewidth is 2 nm in our case, and the first-order SRS power ratio increases rapidly when the seed linewidth deviates from the optimal value. For the ns-SFS seed with a linewidth of less than the optimal value, the intensified fluctuations at the pulse peak result in more severe SRS. On the other hand, for the seed linewidth greater than the optimal width, the wider signal entering the main amplifier contains more Raman band noise than the one at the optimal linewidth and thus causes more severe SRS after power scaling. In addition, by adopting an ns-SFS with a linewidth of 2 nm as the seed, we

https://doi.org/10.1017/hpl.2023.72 Published online by Cambridge University Press

construct an all-fiberized ns-SFS amplifier with a maximum average power of 602 W and a pulse energy of 24.1 mJ. At the maximum output power, the ns-SFS has a pulse width of 57 ns and a corresponding peak power of 422.5 kW. Our study provides valuable insights for further improvements to high-power ns-SFS amplifiers with large pulse energy. Such a laser system offers a promising source for applications such as industrial processing and high-quality full-field imaging of dynamic targets on nanosecond timescales.

Acknowledgements

This work was financially supported by the CAS Project for Young Scientists in Basic Research (No. YSBR-065), the National Natural Science Foundation of China (Nos. 62225507, 62175230, and U2033211), the Scientific Instrument Developing Project of the Chinese Academy of Sciences (No. YJKYYQ20200001) and the National Key R&D Program of China (No. 2022YFB3607800). The authors of this paper would like to thank Professor Jing-Yuan Zhang for his precious time and valuable suggestions in the preparation and revision of the manuscript.

References

1. V. Veiko, Y. Karlagina, M. Moskvin, V. Mikhailovskii, G. Odintsova, P. Olshin, D. Pankin, V. Romanov, and R. Yatsuk, Opt. Lasers Eng. **96**, 63 (2017).
2. T. Heiderscheit, N. G. Shen, Q. H. Wang, A. Samanta, B. X. Wu, and H. T. Ding, Opt. Lasers Eng. **120**, 101 (2019).
3. K. Tsubakimoto, H. Yoshida, and N. Miyanaga, Opt. Lett. **42**, 3255 (2017).
4. L. D. Zhang, J. Y. Zhang, X. Wang, M. Tao, G. T. Dai, J. Wu, Z. W. Miao, S. F. Han, H. J. Yu, and X. C. Lin, Light Sci. Appl. **11**, 12 (2022).
5. F. D. Zhang, H. Liu, C. Suebka, Y. X. Liu, Z. Liu, W. Guo, Y. M. Cheng, S. L. Zhang, and L. Li, Appl. Surf. Sci. **435**, 452 (2018).
6. Y. Liu, W. J. Liu, D. Zhang, Z. Q. Tian, X. W. Sun, and Z. Wei, Appl. Phys. A **126**, 17 (2020).
7. L. Huang, P. F. Ma, D. R. Meng, L. Li, R. M. Tao, R. T. Su, Y. X. Ma, and P. Zhou, High Power Laser Sci. Eng. **6**, e42 (2018).
8. X. C. Chen, N. Wang, C. J. He, and X. C. Lin, Opt. Laser Technol. **157**, 20 (2023).
9. B. N. Upadhyaya, A. Kuruvilla, U. Chakravarty, M. R. Shenoy, K. Thyagarajan, and S. M. Oak, Appl. Opt. **49**, 2316 (2010).
10. W. L. Wang, J. Y. Leng, Y. Gao, S. F. Guo, and Z. F. Jiang, Laser Phys. **25**, 035101 (2015).
11. A. W. Steinforth, J. A. Rivera, and J. G. Eden, APL Phontonics **7**, 016104 (2022).
12. J. M. Xu, P. Zhou, W. Liu, J. Y. Leng, H. Xiao, P. F. Ma, J. Wu, H. W. Zhang, J. B. Chen, and Z. J. Liu, IEEE J. Sel. Top. Quant. **24**, 0900710 (2018).
13. B. Redding, P. Ahmadi, V. Mokan, M. Seifert, M. A. Choma, and H. Cao, Opt. Lett. **40**, 4607 (2015).
14. M. Bashkansky, M. D. Duncan, L. Goldberg, J. P. Koplow, and J. Reintjes, Opt. Express **3**, 305 (1998).
15. A. J. Jin, H. Zhou, X. F. Zhou, J. Hou, and Z. F. Jiang, IEEE Photonics J. **7**, 1600409 (2015).
16. J. Y. Dong, L. Zhang, H. W. Jiang, X. Z. Yang, W. W. Pan, S. Z. Cui, X. J. Gu, and Y. Feng, Opt. Express **26**, 5275 (2018).
17. J. Storteboom, C. J. Lee, A. Nieuwenhuis, I. D. Lindsay, and K. J. Boller, Opt. Express **19**, 21786 (2011).
18. X. Cheng, W. W. Pan, X. Zeng, J. Y. Dong, S. Z. Cui, and Y. Feng, Opt. Fiber Technol. **54**, 102119 (2020).
19. E. J. Park, J. S. Park, H. Jeong, and J. W. Kim, Laser Phys. Lett. **16**, 085108 (2019).
20. J. X. Song, H. S. Wu, S. Ren, W. Liu, P. F. Ma, H. Xiao, and P. Zhou, Opt. Express **29**, 22966 (2021).
21. O. Schmidt, M. Rekas, C. Wirth, J. Rothhardt, S. Rhein, A. Kliner, M. Strecker, T. Schreiber, J. Limpert, R. Eberhardt, and A. Tunnermann, Opt. Express **19**, 4421 (2011).
22. P. F. Ma, L. Huang, X. L. Wang, P. Zhou, and Z. J. Liu, Opt. Express **24**, 1082 (2016).
23. P. Yan, J. Y. Sun, D. Li, X. J. Wang, Y. S. Huang, M. L. Gong, and Q. R. Xiao, Opt. Express **24**, 19940 (2016).
24. J. M. Xu, J. Ye, H. Xiao, J. Y. Leng, W. Liu, and P. Zhou, High Power Laser Sci. Eng. **6**, e46 (2018).
25. Z. Li, G. Li, Q. Gao, P. Wu, S. F. She, Z. L. Wang, N. Huang, C. D. Sun, W. Gao, P. Ju, and H. J. Liu, Opt. Express **28**, 10378 (2020).
26. J. Ye, C. C. Fan, J. M. Xu, H. Xiao, J. Y. Leng, and P. Zhou, High Power Laser Sci. Eng. **9**, e55 (2021).
27. C. Jauregui, J. Limpert, and A. Tunnermann, Nat. Photonics **7**, 861 (2013).
28. T. Schreiber, A. Liem, E. Freier, C. Matzdorf, R. Eberhardt, C. Jauregui, J. Limpert, and A. Tunnermann, Proc. SPIE **8961**, 89611T (2014).
29. W. Liu, P. F. Ma, H. B. Lv, J. M. Xu, P. Zhou, and Z. F. Jiang, Opt. Express **24**, 8708 (2016).
30. V. Bock, A. Liem, T. Schreiber, R. Eberhardt, and A. Tunnermann, Proc. SPIE **10512**, 105121F (2018).
31. C. Y. Ning, S. Z. Zou, H. J. Yu, S. Xu, X. C. Chen, J. X. Zuo, S. F. Han, X. Y. Li, Z. Y. Zhang, C. J. He, and X. C. Lin, Opt. Laser Technol. **157**, 108701 (2023).
32. W. Liu, P. F. Ma, P. Zhou, and Z. F. Jiang, Proc. SPIE **10436**, 104360O (2017).
33. J. Ye, X. Y. Ma, Y. Zhang, J. M. Xu, H. W. Zhang, T. F. Yao, J. Y. Leng, and P. Zhou, Photonics Res. **10**, 618 (2022).
34. X. L. Shen, H. T. Zhang, H. Hao, D. Li, P. Yan, and M. L. Gong, Opt. Express **24**, 4382 (2016).
35. W. Liu, S. Ren, P. F. Ma, and P. Zhou, Chin. Phys. B **32**, 034202 (2023).
36. H. Y. Ying, J. Q. Cao, Y. Yu, M. Wang, Z. F. Wang, and J. B. Chen, Optik **144**, 163 (2017).
37. D. B. S. Soh, J. P. Koplow, S. W. Moore, K. L. Schroder, and W. L. Hsu, Opt. Express **18**, 22393 (2010).
38. W. Liu, P. F. Ma, P. Zhou, and Z. F. Jiang, Laser Phys. Lett. **15**, 025103 (2018).
39. L. M. Frantz and J. S. Nodvik, J. Appl. Phys. **34**, 2346 (1963).
40. D. N. Schimpf, C. Ruchert, D. Nodop, J. Limpert, A. Tunnermann, and F. Salin, Opt. Express **16**, 17637 (2008).
41. C. Jauregui, C. Stihler, and J. Limpert, Adv. Opt. Photonics **12**, 429 (2020).
42. V. Distler, F. Moller, B. Yildiz, M. Plotner, C. Jauregui, T. Walbaum, and T. Schreiber, Opt. Express **29**, 16175 (2021).
43. Q. H. Chu, Q. Shu, Z. Chen, F. Y. Li, D. L. Yan, C. Guo, H. H. Lin, J. J. Wang, F. Jing, C. X. Tang, and R. M. Tao, Photonics Res. **8**, 595 (2020).

https://doi.org/10.1017/hpl.2023.72 Published online by Cambridge University Press